Silicon Nanocrystals Embedded in Nanolayered Silicon oxide for Crystalline Silicon Solar Cells

Ryohei Tsubata[1], *Kazuhiro Gotoh*[1,*], *Masashi Matsumi*[1], *Markus Wilde*[2], *Tetsuya Inoue*[1], *Yasuyoshi Kurokawa*[1], *Katsuyuki Fukutani*[2], *and Noritaka Usami*[1,*]

[1] Department of Materials Process Engineering, Graduate School of Engineering, Nagoya University, Furo-cho, Chikusa-ku, Nagoya 464-8603, Japan

[2] Institute of Industrial Science, The University of Tokyo, 4-6-1, Komaba, Meguro-ku, Tokyo 153-8505, Japan

KEYWORDS: polycrystalline silicon, silicon oxide, silicon nanocrystal, passivation, carrier transport

ABSTRACT

This study describes the fabrication of silicon nanocrystals (Si NCs) in silicon oxide layers, which led to high-performance passivation and enhanced carrier transport in crystalline silicon (c-Si) solar cells. These Si NCs comprised nanocrystalline transport pathways in ultra-thin dielectrics for reinforced passivating contact structures (NATURE contacts). The Si NCs were formed in silicon oxide layers by depositing hydrogenated amorphous silicon oxide (a-SiO_x:H) with different oxygen concentrations, followed by post-deposition annealing (PDA). Based on microscopic images, the silicon oxide layer was maintained after PDA, and the Si NCs were formed in the silicon oxide matrix, leading to a relatively low recombination current (178.8 fA/cm^2) compared with simple a-SiO_x:H layer structures. Furthermore, the contact resistivity for the NATURE contact was 13.1 mΩ·cm^2, which was comparable to that of a single a-SiO_x:H layer with low oxygen concentration. The developed NATURE contact structure expands the design flexibility scope for various functional devices containing a passivation contact layer. It allows for production of c-Si solar cells with passivating contacts using thicker dielectric layers for improved reliability and long-term stability.

INTRODUCTION

Recently, carrier-selective contacts have been studied intensively for their potential to improve the performance of crystalline silicon (c-Si) solar cells.[1] Solar cells containing a stack of doped polycrystalline silicon (poly-Si) and ultra-thin silicon oxide (often called a tunnel oxide passivating contact (TOPCon) or polysilicon on oxide (POLO) junction) exhibit conversion efficiencies exceeding 25%, owing to their high passivation performance and low contact resistance.[2-4] In general, a thick SiO_x film provides excellent passivation[5-7] and is therefore preferable in terms of long-term stability. It is reported that the metal-oxide-semiconductor field-effect transistor (MOSFET) device using thicker silicon oxide than 4 nm suppresses time-dependent dielectric breakdown.[8] This result suggests that solar cells using thicker silicon oxide are more reliable in practical operation. However, the film thickness of the SiO_x in TOPCon and POLO junction solar cells is limited to 1–2 nm to enable the extraction of carriers from crystalline Si because the resistivity of SiO_x is extremely high.[9] The transport of carriers in the poly-Si/SiO_x stack is commonly modeled as tunneling transport[10] or pinhole transport.[11-12] The formation of a carrier pathway (i.e., pinholes) relies on a high-temperature annealing process (above 750 °C), which changes (i) the crystallinity of doped poly-Si, (ii) the dopant diffusion from doped poly-Si, (iii) the bulk lifetime, and (iv) the areal density of the pinholes.[13] The trade-off relationship between surface passivation and carrier transport determines the layer thickness of the insulating SiO_x in TOPCon and POLO junction solar cells. The conductivity of thick SiO_x is beneficial for releasing the solar cells from such a conventional trade-off relationship. Oxygen-alloyed poly-Si passivating contacts have been developed, which achieve good electrical and optical properties.[14-16] Although the oxygen-alloyed poly-Si passivating contacts contain silicon nanocrystals (Si NCs) in the SiO_x matrix, the size of the Si NCs was almost left to nature. Furthermore, the possibility to add

conductivity to thick SiO_x has not been explored. Thick SiO_x may enhance the flexibility of solar cell fabrication through engineered dopant diffusion from doped poly-Si to c-Si by controlling the thickness of the SiO_x and the annealing conditions. Therefore, we propose that the application of a silicon oxide layer containing embedded Si NCs will simultaneously allow high passivation performance and low contact resistivity. Such a NAnocrystalline Transport path in Ultra-thin dielectrics for REinforcing passivating contact (NATURE contact) is illustrated conceptually in Figure 1a, wherein the Si nanocrystals comprise the main carrier transport pathway.

In this paper, we describe the fabrication of multi-stacked structures consisting of hydrogenated amorphous silicon oxide (a-SiO_x:H) films with various oxygen concentrations and post-deposition annealing (PDA) conditions.[17-19] The schematic flow to fabricate the NATURE contact is shown in Figure 1b. During annealing, nearly-spherical silicon crystallites are formed in the silicon-rich layers according to phase separation theories for a multi-stacked system.[20-22] Under optimized annealing conditions, the diameter of the Si nanocrystals corresponds to the layer thickness.[20,23] Overall, the formation of Si NCs could be controlled by the film thickness, the oxygen concentration in the a-SiO_x:H film, and the annealing conditions, and Si NCs in a thick SiO_x layer were prepared via PDA of a 3-layer structure of a-SiO_x:H. This type of structure was expected to improve the conductivity and passivation performance of thicker SiO_x because the carrier transport properties depended on the Si NCs in SiO_x. In this study, we fabricated the proposed structure and investigated its passivation performance and contact resistivity.

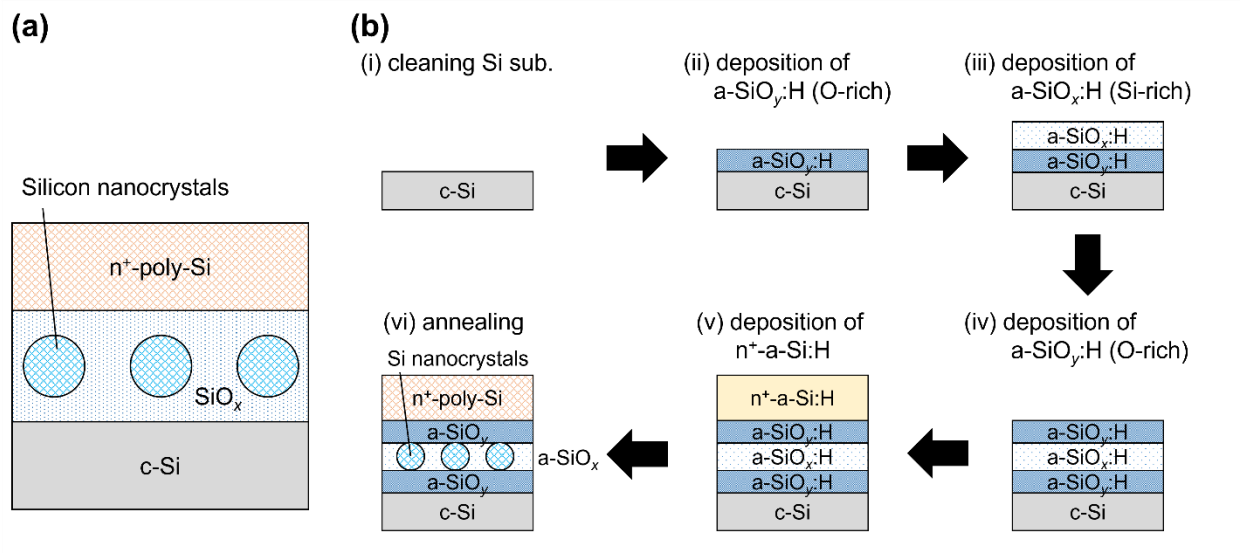

1

2 **Figure 1.** (a) Schematic illustration of the NATURE contact realized by silicon nanocrystals
3 embedded in silicon oxide. (b) The simplified procedure for fabrication of the NATURE contact.

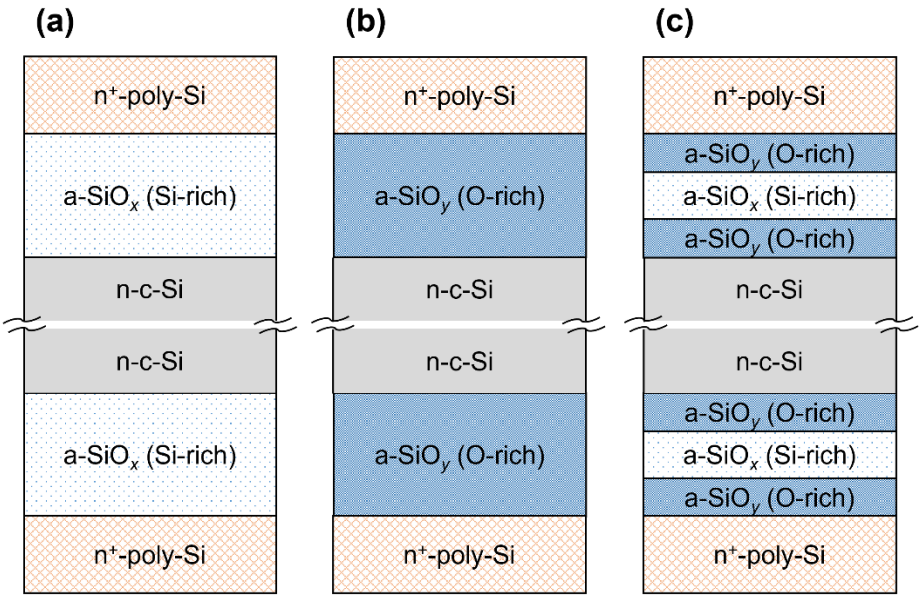

4

5 **Figure 2.** Schematic diagrams of (a) SRO junction, (b) ORO junction and (c) NATURE contact
6 structures.

7

RESULTS AND DISCUSSION

Figures 2a-c show the schematic structures of single a-SiO_x:H layer (silicon-rich oxide (SRO) junction) structures, single a-SiO_y:H layer (oxygen-rich oxide (ORO) junction) structures, and 3-layer structures (NATURE contact). The detailed information about their respective fabrication methods is given in Experimental Methods. The transmission electron microscopy (TEM) images in Figs. 3a and 3b show cross-sections of the SRO and ORO junctions, respectively, after PDA at 750 °C. A lattice fringe was observed in the n^+-a-Si:H layers, indicating that these layers were partially crystallized after PDA. The crystallization of the a-SiO_x layer was observed at the a-SiO_x/c-Si interface (Figure 3a), while no crystallization of the a-SiO_y layer is seen in Figure 3b. Therefore, the a-SiO_y layer suppressed the crystallization from the c-Si substrate. The distinct tolerances to crystallization characteristics of these structures were caused by their different oxygen concentrations.[24] Cross-sectional TEM images of the NATURE contact before and after PDA at 750 °C are shown in Figures 3c and 3d, respectively. Figure 3e shows a magnification of the sample around the NATURE contact after PDA at 750 °C. No lattice fringe is observed in Figure 3c, indicating that the 3-layer structure was amorphous before PDA. However, a lattice fringe was observed in the n^+-a-Si:H layers and a-SiO_x layer, indicating that these layers were partially crystallized. From the diffraction pattern (inset in Figure 3e), the lattice parameter was calculated to be 3.12 Å, which is close to Si(111) spacing. The Si crystals formed in the a-SiO_x layer were nearly spherical and a few nanometers in diameter. This confirmed that Si NCs were successfully generated after annealing the 3-layer structure at 750 °C.

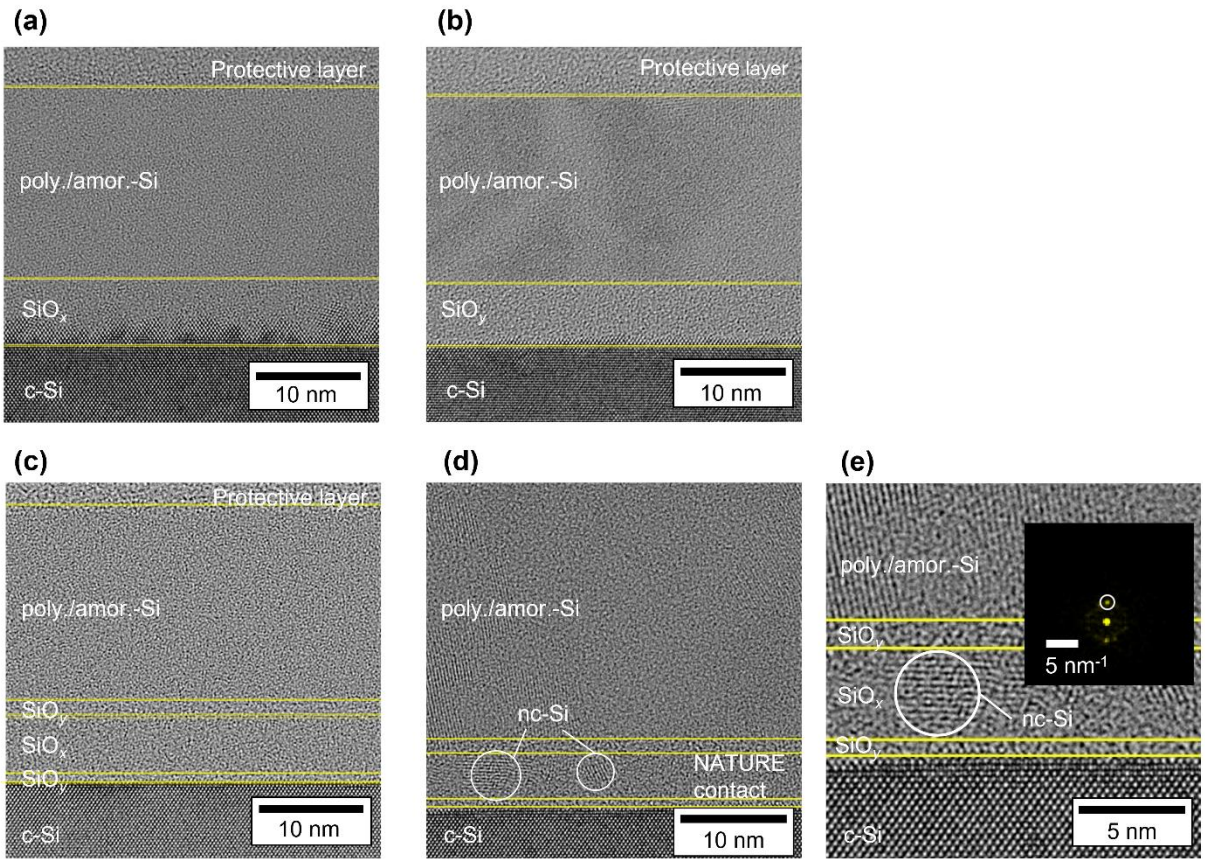

Figure 3. Cross-sectional TEM images of the (a) SRO junction and (b) ORO junction after PDA at 750 °C. Cross-sectional TEM images of the NATURE contact (c) before annealing and (d) after PDA at 750 °C. (e) A magnification of the sample around the NATURE contact after PDA at 750 °C (inset shows the electron diffraction pattern of a Si nanocrystal in the NATURE contact). Yellow lines are guides to the eye for the layered structures.

The injection-dependent effective lifetime (τ_{eff}) curves of the SRO junction, ORO junction, and NATURE contact before and after PDA are presented in Figures 4a and 4b. For as-deposited samples, the τ_{eff} values at the injection level of 1.0×10^{15} cm^{-3} were 1497.3 µs and 369.4 µs for the

SRO junction and ORO junction, respectively. It has been demonstrated that the number of voids in a-SiO:H increases with increasing oxygen content, thus weakening the passivation effect.[25,26]

The τ_{eff} of the SRO junction at 1.0×10^{15} cm^{-3} decreased to 332.8 μs after PDA, whereas that of the ORO junction did not change after annealing relative to the as-deposited sample. The degraded passivation performance of the SRO junction was caused by the crystallization of the a-SiO$_x$ layer (Figure 3a). Accordingly, the maintained passivation of the ORO junction could be attributed to the prevention of crystallization (Figure 3b). Indeed, it has been reported that the crystallization of a-Si:H reduces the passivation performance.[27,28] For the NATURE contact, the τ_{eff} at 1.0×10^{15} cm^{-3} decreased slightly from 727.4 μs to 643.9 μs after PDA. Since no crystallization was observed in this case (Figure 3d), this reduction was likely caused by hydrogen effusion from the bulk a-SiO:H layers and the a-SiO:H/c-Si heterointerface. The thermal equilibrium recombination current density (J_0) values were obtained using Eq. (1),

$$\frac{1}{\tau_{eff}} = \frac{1}{\tau_{bulk}} + 2J_0\frac{N_D}{qn_i^2w} \quad (1)$$

where τ_{bulk} represents the lifetime of Shockley-Read-Hall recombination in bulk c-Si, N_D is the donor concentration, q is the elementary charge, n_i is intrinsic carrier density, and w is the wafer thickness.[29,30] Here, J_0 was calculated using the τ_{eff} at the injection level of 1.0×10^{15} cm^{-3}. The J_0 values for the SRO junction, ORO junction, and NATURE contact were 345.9, 311.6, and 178.8 fA/cm^2. The lowest J_0 value was observed for the NATURE contact, which indicated that this structure should function well as a passivation layer, owing to its suppression of crystallization. The higher J_0 observed for the SRO junction can be explained by the generation of crystallization (Figure 3a). The J_0 value for the ORO junction is likely related to voids in the silicon oxide; as

mentioned previously, the voids in an a-SiO:H layer tend to increase with increasing oxygen content, and this facilitates the recombination of photogenerated carriers.[25,26] It is important to note that the hydrogenation process was not carried out for the NATURE contact. In general, hydrogenation processes, such as remote hydrogen plasma treatment, can be used to enhance the passivation performance because hydrogen is desorbed during PDA, thus reducing the passivation effect.[31-33] The obtained passivation performance of the NATURE contact could be explained by weakened field-effect passivation as well. Kale *et al.* mentioned that the thick silicon oxide layer reduces field-effect passivation.[9] Dopant diffusion in the NATURE contact during PDA seems complicated since the diffusion coefficients in Si and silicon oxide are different. This difference possibly leads to local dopant diffusion and a nonuniform distribution of the in-plane doping concentration. Although the J_0 value of the NATURE contact was still low compared to the conventional TOPCon and POLO junction,[34,35] the τ_{eff} of the NATURE contact was higher than that of a heterostructure using a 1-nm-thick SiO_y layer after PDA at 750 °C (Figure S1). This difference might be caused by suppressed dopant diffusion from n^+-poly-Si to c-Si. Therefore, the NATURE contact can contribute to improving the passivation performance. Further investigation is necessary to clarify the passivation mechanism.

Figure 5 shows γ-ray yield curves as a function of the incident $^{15}N^{2+}$ ion energy (hydrogen depth profiles) measured by nuclear reaction analysis (NRA) from the NATURE contact before and after PDA at 750 °C for 30 min. The vertical black dotted lines in Fig. 5 indicate the surface and heterointerface positions, which were determined from the layer thicknesses obtained in the SE measurements. The inset on the upper part shows the schematic illustration of the samples. In NRA, the NRA γ-ray yield (Y) and $15N^{2+}$ ion energy are correlated to the hydrogen concentration (C_H) and to the depth in the sample, respectively. The details of the NRA technique are given

elsewhere.[36-39] The C_H of the NATURE contact was about 7-8 × 10^{21} cm^{-3} before PDA and fell to the order of 10^{19} cm^{-3} after PDA. The NRA depth profiles revealed that hydrogen was significantly effused out after the PDA, which is responsible for reducing of the passivation performance of the NATURE contact.

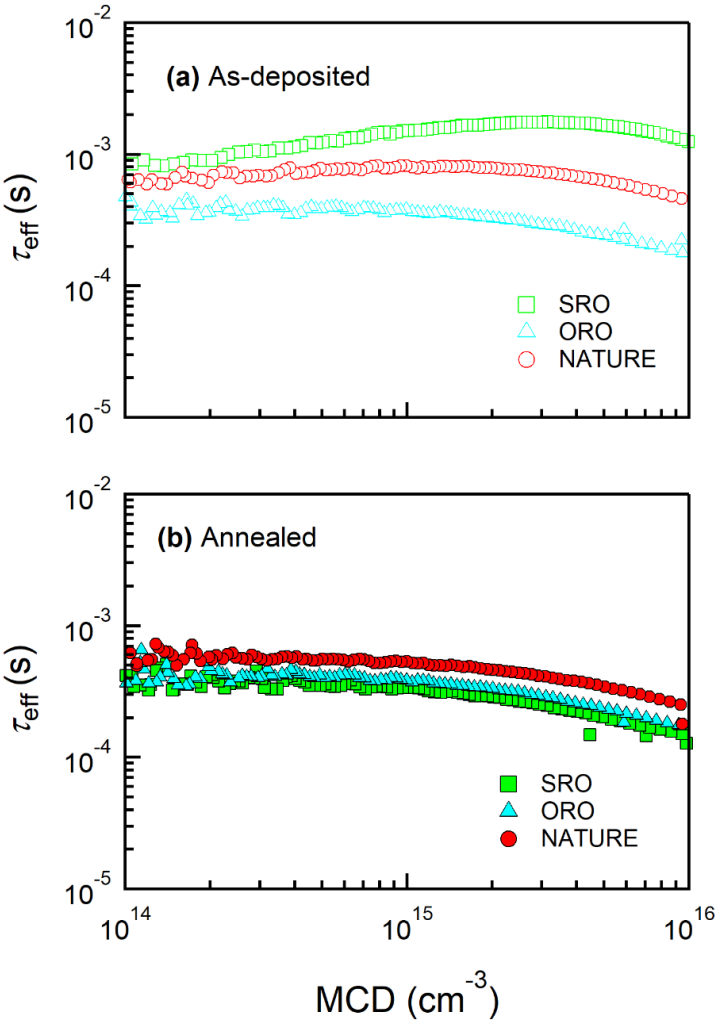

Figure 4. Effective carrier lifetime of SRO junction, ORO junction, and NATURE contact structures (a) before and (b) after annealing, as a function of the minority carrier density (MCD).

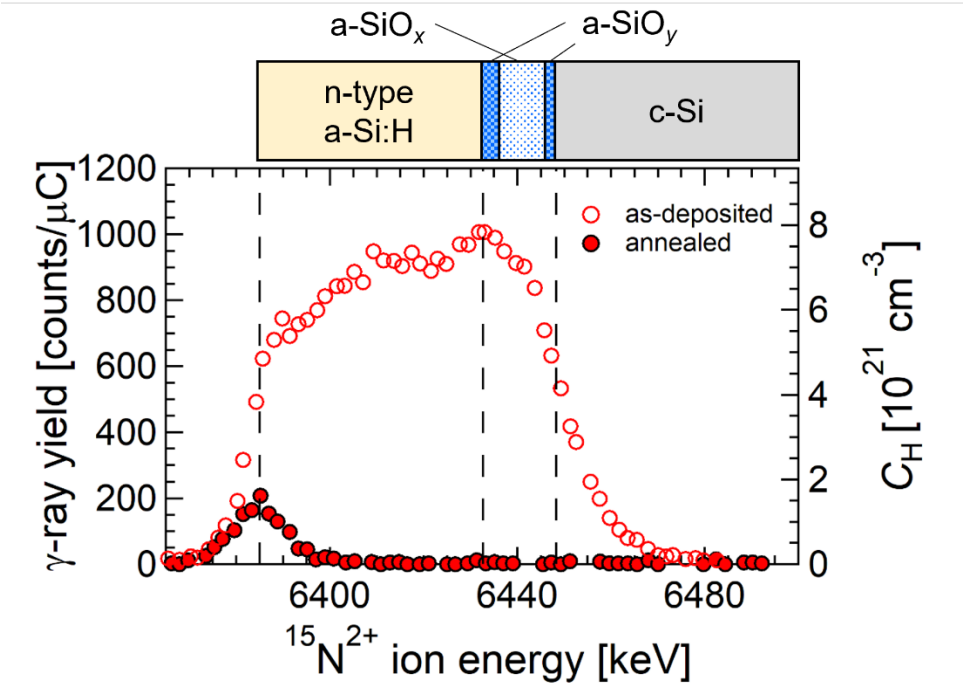

Figure 5. NRA γ-ray yield curves of the NATURE contacts before and after PDA at 750 °C as a function of $^{15}N^{2+}$ ion energy. The vertical black dotted lines indicate the surface and heterointerface positions as determined from the layer thicknesses obtained in SE measurements. The inset on the upper part shows the schematic illustration of the samples.

Figure 6a shows a schematic diagram of the NATURE contact prepared for I-V measurements. Aluminum dot electrodes with different diameters were deposited on one side, and a full-area Al electrode was evaporated on the opposite side. Figure 6b illustrates the linear I-V relationships for the SRO junction and the NATURE contact, and the non-linear I-V relationship exhibited by the ORO junction. The total resistances in the SRO junction, ORO junction, and NATURE contact structures were 1.33 Ω, 4.32 Ω, and 1.42 Ω, respectively. The resistance determined for the ORO junction was extracted in the region from –0.1 to 0.1 V. The higher resistance of the ORO junction

was likely due to the relatively high O content in its a-SiO:H layer. The contact resistivity (ρ_c) values were obtained by applying the Cox-Strack method and using Eq. (2),[40]

$$R_t = R_c + R_s + R_0 = \left(\frac{4R_c}{\pi}\right)\frac{1}{d^2} + \frac{\rho}{\pi}\tan^{-1}\left(\frac{4}{d/t}\right)\frac{1}{d} + R_0 \quad (2)$$

where R_t is the measured total resistance, R_c is the contact resistance, R_s is the spreading resistance, R_0 is the back-side resistance, ρ is the bulk resistivity, d is the diameter of the metal pad, and t is the layer thickness. The ρ_c value was extracted from the slope of a plot of (R_t–R_s) as a function of the inverse electrode area (S^{-1}). Figure 6c shows such a plot for the NATURE contact, and the ρ_c values of the SRO junction, ORO junction, and NATURE contact were 11.9, 45.6, and 13.1 mΩ·cm^2. The SRO junction had the lowest ρ_c, and the ORO junction had the highest ρ_c. The lower value obtained for the SRO junction was attributed to this structure's enhanced carrier extraction caused by the disruption of the a-SiO$_x$, and the higher ρ_c value for the ORO junction was a result of the greater resistivity of a-SiO$_y$. Based on Figure 3b, the a-SiO$_y$/c-Si interface was maintained in the ORO junction, forming an a-SiO$_y$ layer with relatively high O content, which led to high contact resistivity. The ρ_c of the NATURE contact was similar to that of the SRO junction, possibly because of the formation of Si NCs in the a-SiO$_x$.

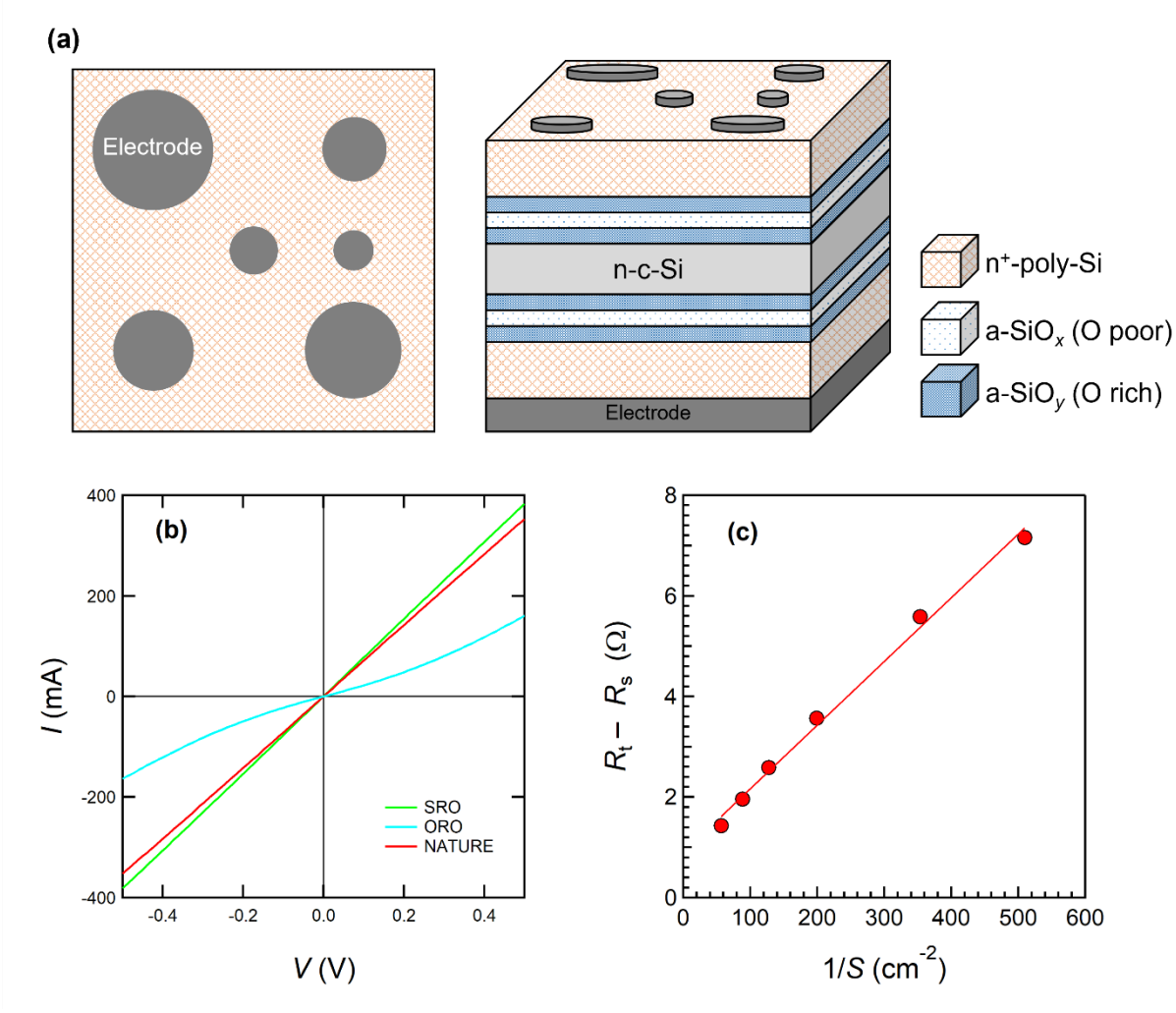

Figure 6. (a) Schematic illustration of the top-view (left) and whole structure (right) of the NATURE contact as prepared for I-V measurements. Aluminum electrodes were thermally evaporated using the Cox-Strack method. (b) I-V characteristics of the SRO junction, ORO junction, and NATURE contact, and (c) R_t–R_s as a function of S^{-1} for the NATURE contact.

The impact of the PDA temperature (T_{anneal}) is shown in Figure 7. Figure 7a shows the dependence of τ_{eff} in the NATURE contact on different T_{anneal} at the injection level of 1.0×10^{15} cm^{-3}. As a rough trend, an increase in the T_{anneal} tends to decrease the τ_{eff}, and it was maximized at

a T_{anneal} of 750 °C. Relatively higher τ_{eff} values were observed for the samples with 4-nm-thick bottom a-SiO_y:H at T_{anneal} = 800 °C, suggesting dopant diffusion into c-Si was suppressed by thicker silicon oxide as mentioned above. The τ_{eff} of samples annealed at high temperatures above 900 °C was significantly lower and nearly constant, since the increase in PDA temperature promoted crystallization of the bottom a-SiO_y:H layer as shown in Fig. 7e. The average τ_{eff} value of 624 μs was obtained in the sample with the bottom a-SiO_y layer thickness of 1 nm and at the PDA temperature of 750 °C due to suppressed crystallization of the bottom a-SiO_y layer.

Figures 7b and 7c show the dependence of J_0 and ρ_c in the NATURE contact with 1-nm-thick bottom a-SiO_y layer on different T_{anneal}. The J_0 and ρ_c values were determined from Eq. (1), and Eq. (2), respectively. An increase in the PDA temperature increases the J_0, which was minimized at a T_{anneal} of 750 °C. The average J_0 value of 184.3 fA/cm^2 was obtained in the sample at the annealing temperature of 750 °C. The ρ_c decreased with increasing annealing temperature. These results can be explained by the promoted crystallization of the silicon oxide layer, formation of the n+-poly-Si layer, increase in activated phosphorous in the n+-poly-Si, and dopant diffusion into c-Si. The ρ_c of the sample annealed at 750 ºC was 13.1 mΩ·cm^2. The value is high in comparison with conventional TOPCon and POLO junctions.[35,35]

Further improvement of the passivation performance of the NATURE contact can be realized by a hydrogenation process after PDA. The τ_{eff} at 1.0×10^{15} cm^{-3} increased from 643.9 μs to 1649.1 μs by hydrogen plasma treatment (HPT) at 400 °C for 30 minutes (Figure S2). The J_0 and ρ_c values of the NATURE contact before and after the hydrogen plasma treatment are summarized in Table S1. Improved J_0 and no significant increase of ρ_c is observed for HP-treated NATURE contact, indicating passivation performance improvement without depression of the carrier transport,

possibly due to hydrogen termination of Si dangling bonds in the NATURE contact. The details of the hydrogenation process applied to the NATURE contact will be reported in the near future.

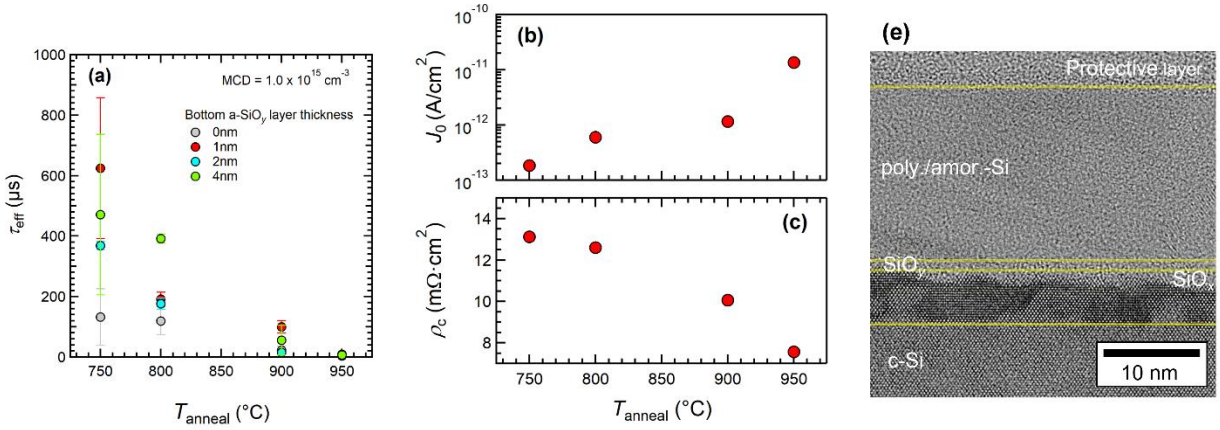

Figure 7. (a) Effective carrier lifetime of the NATURE contact with different thicknesses of the bottom a-SiO_y:H lauer as a function of annealing temperature. Influence of PDA temperature on (b) recombination current density and (c) contact resistivity of the NATURE contact with a 1-nm-thick bottom a-SiO_y:H layer. (d) Cross-sectional TEM images of NATURE contact after PDA at 950 °C. Yellow lines are guides to the eye to highlight the layered structures.

CONCLUSIONS

We fabricated unique NATURE contacts to enhance the conductivity of nanolayered silicon oxide structures. The Si nanocrystals in the oxide layer create carrier transport pathways in the silicon oxide, and cross-sectional TEM images confirmed that the silicon nanocrystals were formed after PDA at 750 °C. The TEM results also revealed that no crystallization occurred at the a-SiO_y:H/c-Si interface along with the formation of Si NCs. Furthermore, relatively low values of

recombination current density J_0 and contact resistance ρ_c (178.8 fA/cm^2 and 13.1 mΩ·cm^2, respectively) were obtained for the NATURE contact, in comparison to other test structures. This demonstrates good passivation performance and conductivity for the relatively thick silicon oxide in the NATURE contact. We propose that further improvements can be attained by implementing a post-PDA hydrogenation process, which would consequently also lead to silicon solar cells with enhanced performance.

EXPERIMENTAL METHODS

Czochralski (CZ) silicon wafers, phosphorus-doped (n-c-Si), 3.1 Ω·cm, 200-μm-thick, polished double sides with surface-oriented (100) was used in this study. All samples were prepared on c-Si substrates via plasma-enhanced chemical vapor deposition (PECVD, ULVAC Inc., CME-200J) with a frequency of 27.12 MHz followed by PDA. The simplified procedure for fabricating Si NC-embedded silicon oxide is shown in Figure 1b. Prior to the deposition of silicon oxide layers, the substrates were cleaned using Semicoclean-23 (Furuuchi Chemicals Co.) for 6 minutes in an ultrasonic bath. The native oxide on the substrates was removed by immersing the substrates in 2.5% HF for 1 min and then dipping them into ozonized, deionized water (DI-O_3) for 10 minutes to clean their surfaces and form a protective oxide layer. Subsequently, the protective oxide layer was stripped off by immersing the material in 2.5% HF for 1 min, after which the substrates were quickly loaded into the PECVD chamber. The a-SiO_x:H was deposited on c-Si substrates using silane (SiH_4) and carbon dioxide (CO_2) gases. The deposition temperature, total pressure, and radio frequency power density were 180 °C, 25 Pa, and 32.5 mW/cm^2, respectively. Two types of a-SiO_x:H were deposited: Si-rich a-SiO_x:H layers and O-rich a-SiO_y:H layers ($x < y$). The gas flow

rates of SiH_4 and CO_2 for a-SiO_x:H were 10 and 10 sccm, respectively, and those for a-SiO_y:H were 6 and 50 sccm, respectively (sccm = standard cubic centimeters per minute). Subsequently, 30-nm-thick n-type hydrogenated amorphous silicon (n^+-a-Si:H) was deposited using SiH_4, hydrogen (H_2), and phosphine (PH_3) gases with flow rates of 40, 400, and 20 sccm, respectively. Three types of samples were fabricated: single a-SiO_x:H layer (silicon-rich oxide (SRO) junction) structures, single a-SiO_y:H layer (oxygen-rich oxide (ORO) junction) structures, and 3-layer structures (NATURE contact), which are depicted in Figure 2a-c. The thickness of the a-SiO_x:H (SRO junction) layer and the a-SiO_y:H (ORO junction) layer were 8 nm. For the NATURE contact, the thickness of the bottom a-SiO_y:H, the middle a-SiO_x:H, and the top a-SiO_y:H layer were fixed at 1 nm, 5 nm, and 2 nm, respectively. The gas flow rates of SiH_4 and CO_2 were changed without interruption to form the 3-layered structures. The layer thickness was controlled by changing the deposition time of a-SiO_x:H and a-SiO_y:H. Forming gas annealing was carried out at 750 °C for 30 min to form n^+-poly-Si and silicon nanocrystals in the a-SiO_x layer using a lamp furnace (ADVANCE RIKO Inc., MILA-5050). For electrical measurements, aluminum electrodes were deposited on the SRO junction, ORO junction, and NATURE contact via vacuum evaporation.

To determine the passivation performance of these materials, the τ_{eff} was measured using quasi-steady-state photoconductance (QSSPC; Sinton Instruments, WCT-120TS) in the generalized 1/1 and 1/64 modes at room temperature.[41] Their contact resistivity (ρ_c) and total resistance were evaluated with I-V measurements using the Cox-Strack configuration.[40,42] The thickness of the layers in each sample was measured using variable-angle spectroscopic ellipsometry (SE; J. A. Woollam, M-2000DI), and the cross-sections of SRO junction, ORO junction, and NATURE contact structures were observed by TEM. Hydrogen depth profiles were measured by NRA via the resonant $^1H(^{15}N,\alpha\gamma)^{12}C$ reaction. The $^{15}N^{2+}$ ion beam of 20-35 nA was generated by the MALT

van de Graaff tandem accelerator at the University of Tokyo. The NRA γ-ray yield (Y) was calibrated to hydrogen concentration (C_H) in a sample by measuring a Kapton reference with a density of 1.45 g/cm^3, a H-concentration of 2.28×10^{22} cm^{-3}, and a stopping power (STP) of 1.2879 keV/nm, which results in a sensitivity constant $\alpha = 1.89 \times 10^{-19}$. C_H values were calculated from as $C_H = Y \times \mathrm{STP}/\alpha$. The STP values of 1.4538 keV/nm was used by assuming the films are crystalline Si, meaning the C_H and the positions of the heterointerfaces were roughly estimated.

ASSOCIATED CONTENT

Supporting Information

Injection-dependent effective lifetime of the n-poly/NATURE contact, the 30-nm-thick n-poly/1-nm-thick SiO_x contact, and the 30-nm-thick n-poly contact after post-deposition annealing at 750 °C; Injection-dependent effective carrier lifetime of the NATURE contact before and after hydrogen plasma treatment.

AUTHOR INFORMATION

Corresponding Authors

* **Kazuhiro Gotoh** - Department of Materials Process Engineering, Graduate School of Engineering, Nagoya University, Furo-cho, Chikusa-ku, Aichi 464-8603, Japan; orcid.org/0000-0002-4877-9370; E-mail: gotoh.kazuhiro@material.nagoya-u.ac.jp

* **Noritaka Usami -** Department of Materials Process Engineering, Graduate School of Engineering, Nagoya University, Furo-cho, Chikusa-ku, Aichi 464-8603, Japan; orcid.org/0000-0002-0602-2847; E-mail: usa@material.nagoya-u.ac.jp

Authors

Ryohei Tsubata - Department of Materials Process Engineering, Graduate School of Engineering, Nagoya University, Furo-cho, Chikusa-ku, Aichi 464-8603, Japan

Masashi Matsumi - Department of Materials Process Engineering, Graduate School of Engineering, Nagoya University, Furo-cho, Chikusa-ku, Aichi 464-8603, Japan

Markus Wilde - Institute of Industrial Science, The University of Tokyo, 4-6-1, Komaba, Meguro-ku, Tokyo 153-8505, Japan; https://orcid.org/0000-0002-6397-2208

Tetsuya Inoue - Department of Materials Process Engineering, Graduate School of Engineering, Nagoya University, Furo-cho, Chikusa-ku, Aichi 464-8603, Japan

Yasuyoshi Kurokawa - Department of Materials Process Engineering, Graduate School of Engineering, Nagoya University, Furo-cho, Chikusa-ku, Aichi 464-8603, Japan; orcid.org/0000-0002-5319-3622

Katsuyuki Fukutani - Institute of Industrial Science, The University of Tokyo, 4-6-1, Komaba, Meguro-ku, Tokyo 153-8505, Japan; https://orcid.org/0000-0002-6270-3620

Author Contributions

All the authors have given approval to the final version of the manuscript.

Funding Sources

This work was financially supported by Japan Society of the Promotion Science (JSPS) KAKENHI Grant number 18H05951, 20K15127, the New Energy and Industrial Technology Development Organization (NEDO) of Japan, 15100646-0, and Grants-in-Aid for Scientific Research on Innovative Areas “Hydrogenomics”, JP18H05514 and JP18H05518.

Notes

The authors declare no competing financial interest.

ACKNOWLEDGMENTS

We thank H. Miura and A. Shimizu for technical support. We also thank Suzanne Adam, PhD, from Edanz Group (https://en-author-services.edanzgroup.com/ac) for editing a draft of this manuscript.

TOC GRAPHIC

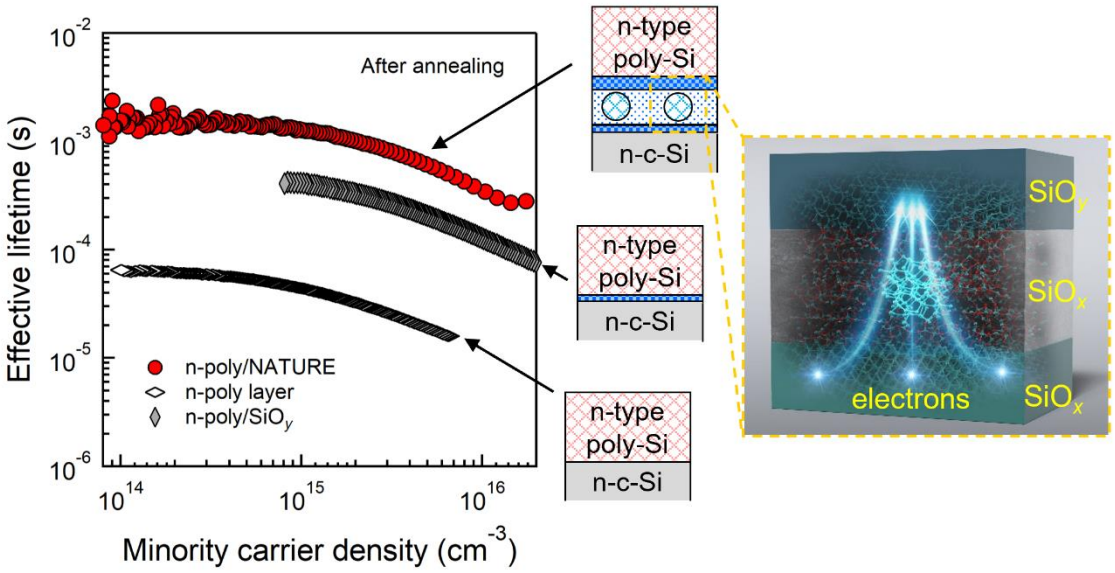

REFERENCES

(1) Melskens, J.; van de Loo, B. H.; Macco, B.; Black, L.; Smit, S.; Kessels, W. M. M. Passivating contacts for crystalline silicon solar cells: From concepts and materials to prospects. *IEEE Journal of Photovoltaics*, **2018**, *8*, 372-388.

(2) Richter, A.; Benick, J.; Feldmann, F.; Fell, A.; Hermle, M.; Glunz, S. W. n-Type Si solar cells with passivating electron contact: Identifying sources for efficiency limitations by wafer thickness and resistivity variation. *Solar Energy Materials & Solar Cells*, **2017**, *173*, 96-105.

(3) Rienäcker, M.; Bossmeyer, M.; Merkle, A.; Römer, U.; Haase, F.; Krügener, J.; Brendel, R.; Peibst, R. Junction resistivity of carrier-selective polysilicon on oxide junctions and its impact on solar cell performance. *IEEE Journal of Photovoltaics*, **2017**, *7*, 11-18.

(4) Haase, F.; Klamt, C.; Schäfer, S.; Merkle, A.; Rienäcker, M.; Krügener, J.; Brendel, R.; Peibst, R. Laser contact openings for local poly-Si-metal contacts enabling 26.1% efficient POLO-IBC solar cells. *Solar Energy Materials & Solar Cells*, **2018**, *186*, 184-193.

(5) Kerr, M. J.; Cuevas, A. Very low bulk and surface recombination in oxidized silicon wafers.

Semiconductor Science and Technology, **2002**, *17*, 35-38.

(6) Nagayoshi, H.; Onozawa, Y.; Ikeda, M.; Yamaguchi, M.; Yamamoto, Y.; Uematsu, T.; Saitoh, T.; Kamisako, K. Effect of hydrogen-radical annealing for SiO_2 passivation. *Japanese Journal of Applied Physics*, **1996**, *35*, L1047-L1049.

(7) Young, D. L.; Nemeth, W.; Grover, S.; Norman, A.; Yuan, H.; Lee, B. G.; LaSalvia, V.; Stradins, P. Carrier selective, passivated contacts for high efficiency silicon solar cells based on transparent conducting oxides. *Energy Procedia*, **2014**, *55*, 733-740.

(8) McPherson, J. W.; Khamankar, R. B. Molecular model for intrinsic time-dependent dielectric breakdown in SiO_2 dielectrics and the reliability implications for hyper-thin gate oxide. *Semiconductor Science and Technology*, **2000**, *15*, 462-470.

(9) Kale, A. S.; Nemeth, W.; Harvey, S. P.; Page, M.; Young, D. L.; Agarwal, S.; Stradins, P. Effect of silicon oxide thickness on polysilicon based passivated contacts for high-efficiency crystalline silicon solar cells. *Solar Energy Materials & Solar Cells*, **2018**, *185*, 270-276.

(10) Steinkemper, H.; Feldmann, F.; Bivour, M.; Hermle, M. Theoretical investigation of carrier-selective contacts featuring tunnel oxides by means of numerical device simulation. *Energy Procedia*, **2015**, *77*, 195-201.

(11) Peibst, R.; Römer, U.; Hofmann, K. R.; Lim, B.; Wietler, T. F.; Krügener, J.; Harder, N.-P.; Brendel, R. A simple model describing the symmetric I-V characteristics of p polycrystalline Si/n monocrystalline Si, and n polycrystalline Si/p monocrystalline Si junctions. *IEEE Journal of Photovoltaics*, **2014**, *4*, 841-850.

(12) Peibst, R.; Römer, U.; Larionova, Y.; Rienäcker, M.; Merkle, A.; Folchert, N.; Reiter, S.; Turcu, M.; Min, B.; Krügener, J.; Tetzlaff, D.; Bugiel, E.; Wietler, T.; Brendel, R. Working principle of carrier selective poly-Si/c-Si junctions: is tunnelling the whole story? *Solar Energy*

Materials & Solar Cells, **2016**, *158*, 60-67.

(13) Lancaster, K.; Großer, S.; Feldmann, F.; Naumann, V.; Hagendorf, C. Study of pinhole conductivity at passivated carrier-selected contacts of silicon solar cells. *Energy Procedia*, **2016**, *92*, 116-121.

(14) Yang, G.; Han, C.; Procel, P.; Zhao, Y.; Singh, M.; Mazzarella, L.; Zeman, M.; Isabella O. Oxygen-alloyed poly-Si passivating contacts for high-thermal budget c-Si heterojunction solar cells. *Progress in Photovoltaics: Research and Applications*, **2021**, 1- 11.

(15) Yang, G.; Guo, P.; Procel, P.; Weeber, A.; Isabella, O.; Zeman, M. Poly-crystalline silicon-oxide films as carrier-selective passivating contacts for c-Si solar cells. *Applied Physics Letter*, **2018**, *112*, 193904.

(16) Stuckelberger, J.; Nogay, G.; Wyss, P.; Jeangros, Q.; Allebé, C.; Debrot, F.; Niquille, X.; Ledinsky, M.; Fejfar, A.; Despeisse, M.; Haug, F-J.; Löper, P.; Ballif, C. Passivating electron contact based on highly crystalline nanostructured silicon oxide layers for silicon solar cells. *Solar Energy Materials and Solar Cells*, **2016**, *158*, 2-10.

(17) Kurokawa, Y.; Tomita, S.; Miyajima, S.; Yamada, A.; Konagai, M. Photoluminescence from silicon quantum dots in Si quantum dots/amorphous SiC superlattice. *Japanese Journal of Applied Physics*, **2007**, *46*, L833-L835.

(18) Kurokawa, Y.; Yamada, S.; Miyajima, S.; Yamada, A.; Konagai, M. Effects of oxygen addition on electrical properties of silicon quantum dots/amorphous silicon carbide superlattice. *Current Applied Physics*, **2010**, *10*, S435-S438.

(19) Akaishi, R.; Kitazawa, K.; Gotoh, K.; Kato, S.; Usami, N.; and Kurokawa, Y. Effect of the niobium-doped titanium oxide thickness and thermal oxide layer for silicon quantum dot solar cells as a dopant-blocking layer. *Nanoscale Research Letters*, **2020**, *15*, 39.

(20) Green, M. A.; Cho, E.-C.; Cho, Y.; Huang, Y.; Pink, E.; Trupke, T.; Lin, A.; Fangsuwannarak, T.; Puzzer, T.; Conibeer, G.; Corkish, R. All-silicon tandem cells based on "artificial" semiconductor synthesised using silicon quantum dots in a dielectric matrix, in *Proceedings of the 20th European Photovoltaic Solar Energy Conference and Exhibition*, Barcelona, **2005**, 3-7.

(21) Chan, J. W. Phase separation by spinodal decomposition in isotropic systems. *Journal of Chemical Physics*, **1965**, *42*, 93-99.

(22) Zhang, L.; Chen, K.; Wang, L.; Li, W.; Xu, J.; Huang, X.; Chen, K. The dependence of the interface and shape on the constrained growth of nc-Si in a-SiNx/a-Si:H/a-SiNx structures. *Journal of Physics: Condensed Matter*, **2002**, *14*, 10083.

(23) Chen, K.; Han, P.; Zou, H.; Ma, Z.; Huang, X. The size control of uniform nanocrystalline Si grains by constrained growth model. *International Journal of Modern Physics B*, **2005**, *19*, 2751-2756.

(24) Chu, Y. H.; Lee, C. C.; Chang, T. H.; Hsieh, Y. L.; Liu, S. M.; Chang, J. Y.; Li, T. T.; Chen, I. C. Investigation of interface quality and passivation improvement with a-SiO:H deposited by ECRCVD at low temperature. *Journal of Non-Crystalline Solids*, **2015**, *412*, 5-10.

(25) Deligiannis, D.; Vliet, J.; Vasudevan, R.; Swaaij, R.; Zeman, M. Passivation mechanism in silicon heterojunction solar cells with intrinsic hydrogenated amorphous silicon oxide layers. *Journal of Applied Physics*, **2017**, *121*, 085306.

(26) Seif, J.; Descoeudres, A.; Filipic, M.; Smole, F.; Topic, M.; Holman, Z.; Wolf, S.; Ballif, C. Amorphous silicon oxide window layers for high-efficiency silicon heterojunction solar cells. *Journal of Applied Physics*, **2014**, *115*, 024502.

(27) Fujiwara H.; Kondo, M. Impact of epitaxial growth at the heterointerface of a-Si:H/c-Si

solar cells. *Applied Physics Letters*, **2007**, *90*, 013503.

(28) Fujiwara, H.; Kaneko, T.; Kondo, M. Application of hydrogenated amorphous silicon oxide layers to c-Si heterojunction solar cells. *Applied Physics Letters*, **2007**, *91*, 133508.

(29) Cuevas, A.; Macdonald, D. Measuring and interpreting the lifetime of silicon wafers. *Solar Energy*, **2004**, *76*, 255-262.

(30) Cuevas A. The Recombination Parameter J_0. *Energy Procedia*, **2014**, *55*, 53-62.

(31) Lindekugel, S.; Lautenschlager, H.; Ruof, T.; Reber, S. Plasma hydrogen passivation for crystalline silicon thin-films, in *Proceedings of the 23rd EUPVSEC*, Valencia, **2008**, 2232-2235.

(32) Mews, M.; Schulze, T. F.; Mingirulli, N.; Korte, L. Hydrogen plasma treatments for passivation of amorphous-crystalline silicon-heterojunctions on surfaces promoting epitaxy. *Applied Physics Letters*, **2013**, *102*, 122106.

(33) Yang, Q.; Liao, M.; Wang, Z.; Zheng, J.; Lin, Y.; Guo, X; Rui, Z.; Huang, D.; Lu, L.; Feng, M.; Cheng, P.; Shou, C.; Zeng, Y.; Yan, B.; Ye, J. In-situ phosphorus-doped polysilicon prepared using rapid-thermal anneal (RTA) and its application for polysilicon passivated-contact solar cells. *Solar Energy Materials & Solar Cells*, **2018**, *210*, 11051.

(34) Schmidt, J.; Peibst, R.; Brendel, R. Surface passivation of crystalline silicon solar cells: Present and future. *Solar Energy Materials and Solar Cells*, **2018**, *187*, 9-54.

(35) Cuevas, A.; Wan, Y.; Yan, D.; Samundsett, C.; Allen, T.; Zhang, X.; Cui, J.; Bullock, J. Carrier population control and surface passivation in solar cells. *Solar Energy Materials and Solar Cells*, **2018**, *184*, 38-47.

(36) Wilde, M.; Fukutani, K. Hydrogen detection near surfaces and shallow interfaces with resonant nuclear reaction analysis. *Surface Science Report*, **2014**, *69*, 196-295.

(37) Fukutani, K. Below-surface behavior of hydrogen studied by nuclear reaction analysis.

Current Opinion in Solid State Materials Science, **2002**, *6*, 153-161.

(38) Gotoh, K.; Wilde, M.; Kato, S.; Ogura, S.; Kurokawa, Y.; Fukutani, K.; Usami, N. Impact of chemically grown silicon oxide interlayers on the hydrogen distribution at hydrogenated amorphous silicon/crystalline silicon heterointerfaces. *Applied Surface Science*, **2021**, *567*, 150799.

(39) Gotoh, K.; Wilde, M.; Kato, S.; Ogura, S.; Kurokawa, Y.; Fukutani, K.; Usami, N. Hydrogen concentration at a-Si:H/c-Si heterointerfaces—The impact of deposition temperature on passivation performance. *AIP Advances*, **2019**, *9*, 075115.

(40) Cox R. H.; Strack, H. Ohmic contacts for GaAs devices. *Solid-State Electronics*, **1967**, *10*, 1213-1214.

(41) Sinton R.; Cuevas, A. Contactless determination of current–voltage characteristics and minority-carrier lifetimes in semiconductors from quasi-steady-state photoconductance data. *Applied Physics Letters*, **1996**, *69*, 2510-2512.

(42) Gupta, R. P.; White, J. B.; Iyore, O. D.; Chakrabarti, U.; Alshareef, H. N.; Gnade, B. E. Determination of contact resistivity by the Cox and Strack method for metal contacts to bulk bismuth antimony telluride. *Electrochemical and Solid-State Letters*, **2009**, *12*, H302-H304.